Extreme Mechanics Letters 38 (2020) 100746

Contents lists available at ScienceDirect

Extreme Mechanics Letters

journal homepage: www.elsevier.com/locate/eml

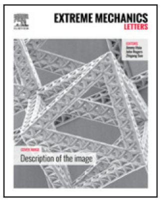

Hygroresponsive coiling of seed awns and soft actuators

Jonghyun Ha, Sung Mok Choi, Beomjune Shin, Minhee Lee, Wonjong Jung, Ho-Young Kim [*]

Department of Mechanical and Aerospace Engineering, Seoul National University, Seoul 08826, Republic of Korea

ARTICLE INFO

Article history:
Received 13 January 2020
Received in revised form 12 April 2020
Accepted 20 April 2020
Available online 23 April 2020

Keywords:
Composite plates
Botanical movements
Coiling motion
Soft actuators

ABSTRACT

The seeds of *Pelargonium* species possess a long slender appendage called an awn, which enables self-burial of the seeds into soil by helically coiling in response to environmental humidity change. Here we analyze morphology of the helix formed by the awn, and fabricate artificial hygroresponsive helical actuators by depositing aligned nanofibers, and show that our theory agrees well with the experimental results of both the biological and the artificial actuators. To go beyond previous analysis of individual cell deformation, which cannot predict the overall awn shape, we model the awn as a trilayer structure consisting of two active sublayers and one inactive layer by noting that the inextensible microfibrils coiling individual active cells are tilted at constant angles in each sublayer. The laminated composite anisotropic plate theory allows us to predict the shape of the biological and artificial helices as a function of the mechanical properties, the layer thickness, the fiber tilt angle, and the environmental humidity. Our tissue-level understanding of the biological actuator and cost-effective nanofabrication schemes can lead to soft actuators capable of versatile helical deformation driven by external stimuli.

Contents

1. Introduction

Soft actuators that can respond to environmental stimuli including light, heat and humidity play important roles in soft robotics, [1] energy harvesting, [2] and fabrication of reconfigurable objects [3]. Plants, which are capable of motion without complex motor proteins of muscle, provide rich source of inspirations for simple but versatile soft actuation systems. Most of botanical movements rely on transport of water whether it is driven by osmosis, cell growth or external change of moisture concentration. Considering the fundamental response modes of plant tissues, the botanical motions are categorized to be dominated by either swelling or elastic instabilities [4]. Some of the examples explained by the swelling and shrinking due to turgor pressure change of plant cells include the opening and closure of stomata [5] and the angular motion of *Mimosa pudica* leaves [6]. Elastic instabilities are responsible for the rapid closure of snapping Venus flytrap [7] and the explosive seed dispersal from fractured fruit of *Hura crepitans* [8].

Even without relying on turgor pressure change, plants can generate motions hydraulically owing to environmental humidity change, as evidenced by the folding of dry pollen grain surfaces, [9] the bending of pine cones [10] and wild wheat awns, [11] and the chiral deformation of seed pods of *Bauhinia variegate* [12]. Here, we are interested in analyzing and mimicking the

---

[*] Corresponding author.
E-mail address: hyk@snu.ac.kr (H.-Y. Kim).

https://doi.org/10.1016/j.eml.2020.100746
2352-4316/© 2020 Published by Elsevier Ltd.

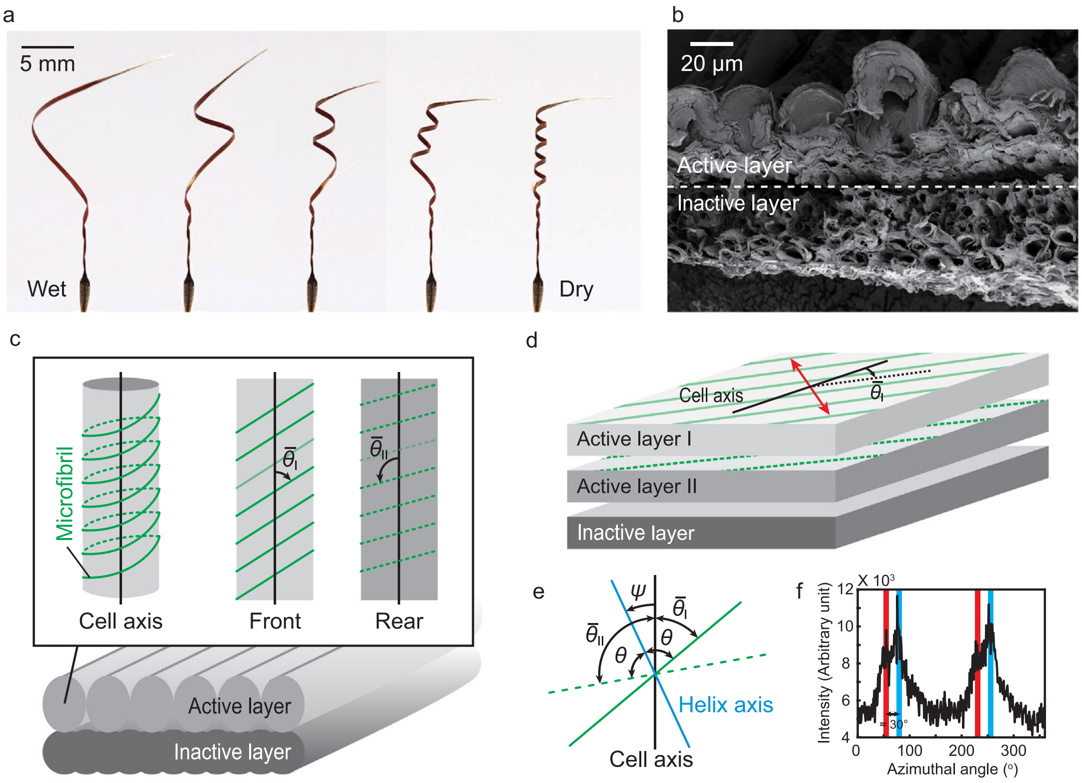

Fig. 1. Characteristics of *Pelargonium appendiculatum* seed awns (see Movie S1). (a) Coiling motion of the seed awn with change of relative humidity. (b) Microscopic image of the cross-section of the awn. (c) Schematics of the bilayer structure of the awn. The box shows a single cell of the awn coiled by tilted cellulose microfibrils. (d) A simplified model of the awn decomposed into trilayers. $\bar{\theta}_{\mathrm{I}}$ is MFA of active layer I. Red arrows indicate directions of hygroscopic expansion perpendicular to microfibrils. (e) Description of the angles defining the microstructure of the awn. Here, $\bar{\theta}_{\mathrm{I}}$ and $\bar{\theta}_{\mathrm{II}}$ are measured in clockwise and counterclockwise directions, respectively, from the cell axis. (f) The SAXS intensity plotted as a function of the azimuthal angle of a hygroscopically active cell of *Pelargonium appendiculatum* seed awn, which was oriented perpendicular to the direction of beam. The red and blue lines correspond to $\bar{\theta}_{\mathrm{I}} = 55°$ and $\bar{\theta}_{\mathrm{II}} = 85°$, respectively. The line width indicates the uncertainty of measurement, ±5°. (For interpretation of the references to color in this figure legend, the reader is referred to the web version of this article.)

motion strategy of seed awns of *Pelargonium*. The awns are coiled when dry but uncoil to stretch with the increase of humidity, which rotate and propel the seeds into ground for germination [13–16]. The awn, a long tail of seed, consists of two layers, one of which (active layer) deforms in response to environmental humidity change while the other (inactive layer) not [17]. Individual cylindrical cells constituting the active layer are known to be wound by crystalline cellulose microfibrils that form a titled helix [18]. Although the geometry and mechanics of the simultaneous bending and twisting of those individual cells were elucidated, [19] such a cellular-level approach cannot predict the morphology change of actual awns. The mechanical analysis of the collective behavior of the active layer made of hundreds of those cells and the inactive layer has not been attempted yet for complexity of the problem. Such investigation of tissue level would not only allow us to fully understand the motion principle of the botanical actuators, but also lead to design, fabrication and control of artificial systems to perform helical coiling as powered by humidity change.

Here we start with biomechanical study of actual seed awns and then apply the results to analyze, design and fabricate seed-mimicking soft actuators. We first describe experiments to observe and measure the helical motion of *Pelargonium* seed awns. We construct a theoretical model to explain the tissue-level behavior of the awns, and compare the results with the experiment measurements. We then move on to fabrication of artificial actuators whose structure is inspired by the seed awns to perform helical coiling. We finally compare the theoretical prediction and the experimental measurements of morphological responses of the artificial actuators to humidity change.

2. Results and discussion

2.1. Biological observation

To investigate the helical motions of seed awns, we use seeds of *Pelargonium appendiculatum*. Upon placing a seed in a thermo-hygrostat at 25°, we decrease the relative humidity (RH) from 95 to 50% for 30 min, and observe the initially uncoiled awn to coil as pictured in Fig. 1a. The coiled awn was uncoiled reversibly when RH was increased. We measure the radius (R) and the pitch (P) of the helix made by each awn, and the average values (± standard deviations) of the five awns were $R = 0.90 \pm 0.43$ mm and $P = 1.85 \pm 0.24$ mm when RH = 50%.

Fig. 1b shows a bilayer structure of the cross-section of the awn, where the upper layer is arranged with cylindrical cells exhibiting a great degree of morphological variation in response to humidity change. The lower one is insensitive to humidity. The cell walls are in general composed of hemicellulose and lignin that swell upon absorbing moisture. The walls of cells in the active layer are coiled by tilted cellulose fibers, called microfibrils, as shown in Fig. 1c [20]. As the polymers in the cell wall can swell only in a direction perpendicular to the microfibrils, the individual active cells bend and twist simultaneously, or helically coil, in response to humidity change [21]. The walls of cells in the inactive layer are tightly bound by microfibrils, thereby exhibiting negligible hygroscopic deformation [22].

2.2. Theoretical model

To explain the overall awn deformation, we go beyond the prior analysis [19] of individual cell's deformation and analyze the tissue-level morphology change. Instead of directly computing the awn shapes considering hundreds of individual active cell's deformation as constrained by the inactive layer, we conceptually decompose the active layer into two sublayers as shown in Fig. 1d. The upper surfaces of the cells constituting layer I share the same microfibril angle (MFA, the angle between the longitudinal axis of the plant cell and the direction of the helical windings of microfibrils), $\bar{\theta}_{\mathrm{I}}$. The lower surfaces of the cells constituting layer II share the microfibril angle, $\bar{\theta}_{\mathrm{II}}$. Then the awn can be simply modeled as a trilayer structure having two active layers and one inactive layer. Each active layer has an array of microfibrils that are tilted by MFA, $\bar{\theta}_{\mathrm{I}}$ or $\bar{\theta}_{\mathrm{II}}$, with respect to the cell axis, so that the layer can expand or shrink only in a direction perpendicular to the microfibrils.

To theoretically describe the helical shapes resulting from deformation of the trilayer, we define the tilt angle of microfibrils, ψ, as shown in Fig. 1e. For a non-tilted helix, $\bar{\theta}_{\mathrm{I}}$ and $\bar{\theta}_{\mathrm{II}}$ are equal. A difference of $\bar{\theta}_{\mathrm{I}}$ and $\bar{\theta}_{\mathrm{II}}$ of tilted helices can be understood by the tilting of the helix axis relative to the cell axis by ψ. Therefore, the microfibril angles of the front (upper) and rear (lower) microfibrils with respect to the helix axis are commonly θ, so that $\bar{\theta}_{\mathrm{I}} = \theta - \psi$ and $\bar{\theta}_{\mathrm{II}} = \theta + \psi$. The deformation of each active layer is anisotropic as confined by the microfibril angles.

The microfibril angles can be measured by the method of small angle X-ray scattering (SAXS) [23]. Using the SAXS spectrometer (Xenocs, Xeuss 2.0), we obtained the SAXS pattern of a cell in the active layer of the seed awns of *Pelargonium appendiculatum*, which is similar to the pattern of a different species of the same genus, *P. peltatum* [24]. The integration of intensity from the SAXS pattern as shown in Fig. 1f allows us to find two microfibril angles, $\bar{\theta}_{\mathrm{I}} = 55^\circ$ and $\bar{\theta}_{\mathrm{II}} = 85^\circ$ with the uncertainty of measurement $\pm 5^\circ$. Then we obtained $\theta = 70^\circ$ and $\psi = 15^\circ$.

Fig. 2a shows the multilayer structure identical to the awn model of Fig. 1d. The longitudinal axis of the strip in Fig. 2a coincides with the cell axis in Fig. 1e, and we take the helix axis as the y-axis. In active layer I, the reference coordinate (x, y) should rotate counterclockwise by $\pi/2 - \theta$ to coincide with the material coordinates $(1, 2)$. In active layer II, the reference coordinates should rotate clockwise by $\pi/2 - \theta$ to coincide with the material coordinates. Our goal in the analysis of the awn is to find geometrical parameters, radius R and pitch P, that define the helix ribbon, as a function of RH.

In view of small thickness (70 μm) of the awns relative to their length (20 mm) and width (0.7 mm), we employ a theory of laminated composite plates, where only the thickness participates among geometrical parameters [25]. The deformation tendencies of the plates depend on the stress, and a simple constitutive relation can be expressed as $\sigma = C\epsilon$, where σ, C, and ϵ are respectively the stress, the elastic modulus, and the total strain. The total strain at a distance z from the midplane is given by $\epsilon = \epsilon_0 + \kappa z$ under the Kirchhoff assumption, [26] where ϵ_0 is the midplane strain and κ is the curvature. The constitutive relation $\sigma = C(\epsilon_0 + \kappa z)$ leads to the matrix equations of the forces $\mathbf{N}$ and moments $\mathbf{M}$: $\mathbf{N} = \boldsymbol{A}\boldsymbol{\epsilon}_{\mathbf{0}} + \boldsymbol{B}\boldsymbol{\kappa}$ and $\mathbf{M} = \boldsymbol{B}\boldsymbol{\epsilon}_{\mathbf{0}} + \boldsymbol{D}\boldsymbol{\kappa}$, where $\boldsymbol{A}$, $\boldsymbol{B}$ and $\boldsymbol{D}$ are the mechanical properties of the composite materials (see Supplementary Material S1 for details). Bold symbols correspond to the matrices.

We note that $\mathbf{N}$ and $\mathbf{M}$ are induced by hygroscopic swelling, not by external stress as elaborated on in Supplementary Material S2. The stress induced by hygroscopic swelling can be written as $\sigma_h = C\alpha\Delta\phi$, where α is the hygroscopic swelling coefficient and $\Delta\phi = \phi_s - \phi$ is the difference between the current moisture concentration (ϕ) and the saturation concentration. In a perfectly dry state ($\phi = 0$), σ_h is maximized and the awn is coiled to the maximum degree. As ϕ increases, σ_h decreases, leading to uncoiling of the awn and thus increase of R and P. The awn is completely stretched when the awn is fully wetted or $\Delta\phi = 0$.

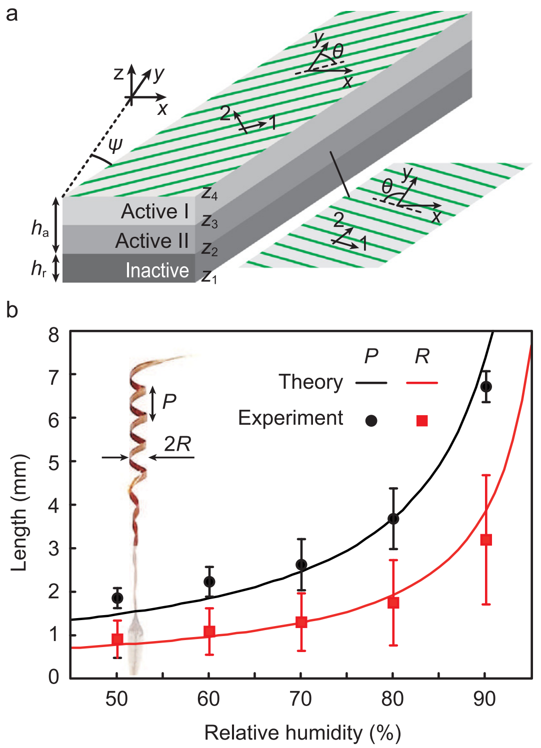

Fig. 2. Laminated composite plate model of the seed awn. (a) Schematics of the anisotropic composite plates. Numbers 1 and 2 correspond to the material coordinates. The major expansion occurs along the 2-axis. h_a and h_r denote the thickness of the active and inactive layers, respectively. The thicknesses of the two active sublayers I and II are the same. (b) Radius (R) and pitch (P) of the seed awn as a function of RH. Mechanical properties and awn's geometrical parameters are listed in Supplementary Material S3. The error bars of the data correspond to the standard deviation for five samples.

For anisotropic plates, the direction of hygroexpansion is determined by θ in Fig. 2a. Once ϕ and the mechanical properties are given, we can calculate the reference curvature tensor $\bar{\boldsymbol{b}}$:

$$\bar{\boldsymbol{b}} = \begin{bmatrix} \kappa_1 & 0 \\ 0 & \kappa_2 \end{bmatrix}, \tag{1}$$

where κ_1 and κ_2 are the eigenvalues of the curvature tensor (Supplementary Material S2). The maximum value of κ_1 and κ_2 becomes the principal curvature, κ_0, which determines the helix shape. The radius R and the pitch P of the helix is given by κ_0 and ψ as $R = 1/\kappa_0$ and $P = 2\pi \tan\psi/\kappa_0$. [12] Because κ_0 is a function of $\Delta\phi$, we find R and P of the seed awn of *Pelargonium appendiculatum*, whose mechanical properties and geometric parameters are given in Supplementary Material S3, as a function of RH. The results are plotted in Fig. 2b. Fairly good agreement between our theoretical predictions and the experimental measurements of R and P, shown in Fig. 2b, verifies our trilayer assumption in modeling the hygroscopic deformation of the seed awns.

2.3. Fabrication of hygroresponsive nanofibrous sheets

Inspired by the *Pelargonium* seed awns that exhibit helical coiling, we fabricate artificial actuators capable of helical deformation in response to environmental humidity change. Because the awn's coiling is owing to anisotropic expansion of plates in a direction tilted from the major axis, we reproduce such directional expansion using sheets formed by aligned fibers. The hygroscopically responsive fibrous sheets are produced by the directional electrospinning process [27].

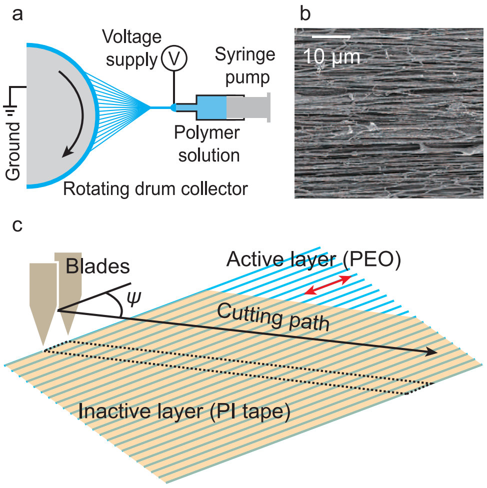

Fig. 3. Hygroresponsive helical soft actuators. (a) Directional electrospinning process to fabricate a bilayer comprising a hygroresponsive layer of aligned PEO nanofibers and an inactive PI layer. (b) Scanning electron microscopy image (top view) of the active layer with aligned PEO nanofibers. (c) Cutting of the bilayer at an angle ψ from the fiber alignment (blue lines) to obtain a coiling soft actuator. The red arrow indicates the direction of hygroscopic expansion. (For interpretation of the references to color in this figure legend, the reader is referred to the web version of this article.)

The process is schematically illustrated in Fig. 3a, where a strong electrical field is applied to a polymer solution drop hanging from a capillary needle. A nanojet is issued from the drop due to strong electrical repulsion at the drop surface, and then is deposited on a rotational collector as partially solidified during flight. By matching the rotational speed (2000 rpm) of the collector 9 cm in diameter to the jet speed, the whipping instability of the electrified jet [28] is suppressed and the nanofibers are aligned on the collector as imaged in Fig. 3b. The effects of the rotational speed of the collector on fiber alignment and consequent actuation performance are discussed in Supplementary Material S4.

As the polymer solution, we use 10 wt% aqueous PEO (polyethylene oxide with the viscosity-average molecular weight 3×10^5 g/mol, Sigma Aldrich). The distance and voltage between the collector and the needle tip of the inner diameter of 260 μm is 15 cm and 10 kV, respectively. We obtain a fibrous sheet of 40 μm thickness upon electrospinning for 3 h, which is detached from the collector by being adhered to a PI (polyimide) film of 50 μm in thickness as depicted in Fig. 3a. It was found that the diffusion of water molecules in fibrous sheets of PEO is more effective than that in a dense layer, [29] so that the effective diffusion coefficient of the fibrous sheets is 9×10^{-11} m^2/s while that of spin-coated layers is 1.2×10^{-12} m^2/s. This enhanced diffusion rate leads to a fast response of our artificial actuators to humidity change.

The resulting bilayer consists of a hygroscopically active PEO nanofibrous layer and a hygroscopically inactive PI layer. The major difference between the green lines in Fig. 1, microfibrils, and the blue lines in Fig. 3, nanofibers, is that the plate expands in a direction perpendicular to the microfibrils but parallel to the nanofibers. To finally obtain a helically coiling actuator, we cut the bilayer along a line that is tilted from the alignment of nanofibers. The tilt angle indicated in Fig. 3c corresponds to the angle between the plate expansion direction and the major axis of strip. We see that it is equivalent to the angle ψ in Fig. 1e, which is an angle between the cell expansion direction (helix axis) and the major axis of the awn parallel to the cell axis. Thus, the cutting angle in Fig. 3c is also denoted by ψ.

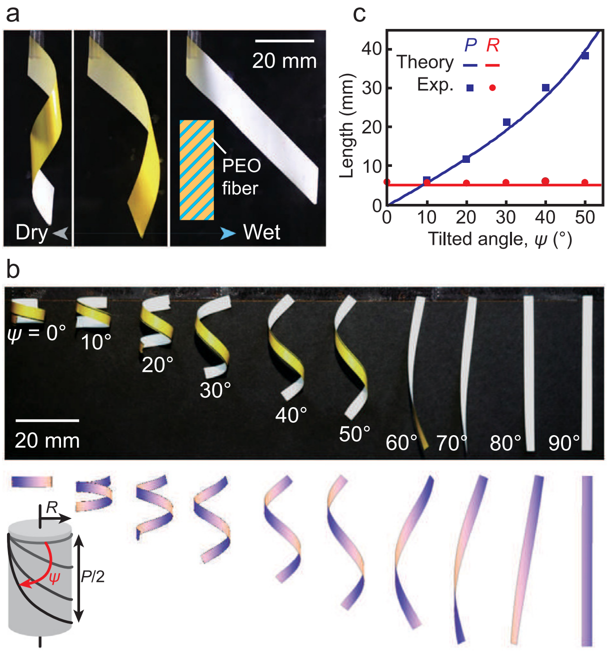

Fig. 4. (a) The helical deformation of the hygroscopic actuator with $\psi = 45°$. RH of the left, middle, and right panels is 20, 50, and 70%, respectively (see Supplementary Movie S2). (b) Experimental images of the fabricated actuators (top) and computational results of the actuators (bottom) with different ψ at RH of 20%. Inset: virtual helix geometry. (c) Radius R and pitch P of the actuators versus ψ.

2.4. Helical deformation of actuators

Fig. 4a shows the deformation of the artificial bilayer actuator with $\psi = 45°$. The initially coiled bilayer in a dry condition is stretched out as the relative humidity increases owing to expansion of PEO fibers. Drying the actuator reversibly coils the strip as the aligned fibers are contracted while tilted from the major axis. Although our artificial actuators consist of two layers one of which is hygroscopically active, they are capable of helical deformation as versatile as the *Pelargonium* seed awns virtually having two active layers. That is, by tuning the stiffness and thickness of the active and inactive layers and the fiber tilt angle ψ in the bilayer, one can obtain the same R and P as those achieved in any multi-layered actuators.

The helical deformation of the artificial bilayers can be analyzed by the theory developed for the above biological actuators. The reference curvature tensor $\bar{\boldsymbol{b}}$ in Eq. (1) is again obtained by the laminated composite plate theory as delineated in Supplementary Material S2, which allows us to find the radius and the pitch of the helically coiled actuator as a function of RH, thickness and stiffness of the layers, and fiber tilt angle. Fig. 4b compares the experimental images of the actuators with varying ψ with the theoretically computed shapes of the actuators. The mechanical properties and the actuator dimensions are listed in Supplementary Material S3. When $\psi = 0$, the hygroresponsive fibers are aligned with the major axis of the strip, implying that the bilayer corresponds to a simple bending actuator. As ψ increases, the pitch of the helix increases while the radius hardly changes until ψ increases to 50°. For $\psi > 50°$, the pitch becomes longer than the current ribbon with a length of 50 mm. When ψ reaches 90°, the fibers are perpendicular to the major axis, so that the bilayer merely curls about the major axis.

In Fig. 4c, we quantitatively compare the theoretical predictions of R and P, as a function of ψ with the experimental results, to find good agreement between them. We see that R is independent of ψ once the mechanical properties (elastic moduli and hygroscopic expansion coefficients) and the dimensions (h, θ) of the actuators and RH are fixed. It is because ψ plays no role in determining the curvature tensor $\bar{\boldsymbol{b}}$. The inset of Fig. 4b shows that the helix shape is determined by the oblique lines oriented by ψ on a cylinder with fixed $R = 1/\kappa_0$. In Supplementary Material S5, we additionally present the computational results of R and P as a function of the thickness of the active and the inactive layer. These results imply that we can tune the design parameters (ψ and layer thickness) of the hygroresponsive soft actuators to achieve the desired shapes of helices based on our theory.

The hygroscopic actuation is driven by diffusion of water molecules into an active layer. Thus, we can estimate the characteristic time of actuation by considering the characteristic time for water molecule diffusion into the active layer: $\tau \sim h_a^2/D$ with h_a being the active layer thickness and $D \approx 9 \times 10^{-11}$ m^2/s the effective diffusion coefficient of water molecules in fibrous PEO layer [29,30]. For $h_a = 40$ μm in our experiments, we get $\tau \approx 20$ s, which is consistent with our observation that it takes approximately 30 s for the bilayer actuator to completely coil from a fully stretched state with drying or to completely uncoil from a fully coiled state with wetting. In practical applications, a significant degree of coiling can be obtained within a few seconds because a partially wetted active layer still can lead to helical coiling of the bilayer. For instance, it takes only ∼1 s for water molecules to diffuse as far as a quarter of the active layer thickness because $\tau \sim (h_a/4)^2/D \sim 1$ s.

3. Conclusions

The awns of *Pelargonium* seeds can coil in response to change of environmental humidity owing to tilted helix of inextensible cellulose microfibrils around the cells constituting the hygroscopically active layer of the awns. Although the hygroscopic deformation of those single cells constrained by the microfibrils was previously analyzed, the behavior of the individual cells is not directly linked to the overall helical shape of the awn composed of layers of active and inactive cells. Therefore, we have constructed a theoretical model to analyze the hygroresponsive actuation of the entire awn. We have modeled the awn as a trilayer structure consisting of two active sublayers and one inactive layer by noting that the microfibrils on the upper and lower faces of the aligned active cells are tilted at constant angles from the cell axis. Then the theory of laminated composite anisotropic plates allows us to predict radius and pitch of helices formed by hygroscopic deformation of the entire awn, which agree well with experiment. We have further fabricated hygroresponsive awn-inspired actuators via the directional electrospinning process. We have shown that the artificial bilayers consisting of one active and one inactive layer can exhibit the helical coiling just as the awns. Even with the bilayers with the same mechanical strength and dimensions, we can obtain different helix shapes by changing the tilt angle of fiber alignment with respect to the major axis of the long strip.

The success of our model in predicting the helical deformation of the *Pelargonium* seed awns is attributed to the monolayer arrangement of active cells, which allows us to assume the awn to be a trilayer. Unlike *Pelargonium* species, *Erodium* species are known to have the hygroresponsive seed awns whose active layer consists of multilayer stacks of active cells [18]. A further theoretical endeavor is called for to come up with a model to analyze the tissue-level deformation of the *Erodium* seed awns having such microstructure of significant complexity. Upon the basis of our precise knowledge of the relationship between the microstructure of fibrous actuators and their overall morphing behavior, a novel soft actuator may be possible which can actively control its deformation mode by adjusting its microstructure, such as the fiber alignment angle. Direct applications of our helically morphing bilayer include a self-burrowing actuator that can propel itself into soil just as its biological counterpart, *Pelargonium* seeds (Supplementary Material S6).

Declaration of competing interest

The authors declare that they have no known competing financial interests or personal relationships that could have appeared to influence the work reported in this paper.

Acknowledgments

We are grateful to Prof. Anna Lee for helpful comments. This work was supported by National Research Foundation of Korea (Grant No. 2018-052541 and 2019R1A6A3A03032230) via SNU IAMD.

Appendix A. Supplementary data

Supplementary material related to this article can be found online at https://doi.org/10.1016/j.eml.2020.100746.

References

[1] L. Hines, K. Petersen, G.Z. Lum, M. Sitti, Soft actuators for small-scale robotics, Adv. Mater. 29 (2017) 1603483, http://dx.doi.org/10.1002/adma.201603483.

[2] M. Ma, L. Guo, D.G. Anderson, R. Langer, Bio-inspired polymer composite actuator and generator driven by water gradients, Science 339 (2013) 186–189, http://dx.doi.org/10.1126/science.1230262.

[3] L. Ionov, Biomimetic hydrogel-based actuating systems, Adv. Funct. Mater. 23 (2013) 4555–4570, http://dx.doi.org/10.1002/adfm.201203692.

[4] J.M. Skotheim, L. Mahadevan, Physical limits and design principles for plant and fungal movements, Science 308 (2005) 1308–1310, http://dx.doi.org/10.1126/science.1107976.

[5] I. Zelitch, Biochemical control of stomatal opening in leaves, Proc. Natl. Acad. Sci. USA 47 (1961) 1423, http://dx.doi.org/10.1073/pnas.47.9.1423.

[6] K. Song, E. Yeom, S.J. Lee, Real-time imaging of pulvinus bending in Mimosa pudica, Sci. Rep. 4 (2014) 6466, http://dx.doi.org/10.1038/srep06466.

[7] Y. Forterre, J.M. Skotheim, J. Dumais, L. Mahadevan, How the Venus flytrap snaps, Nature 433 (2005) 421–425, http://dx.doi.org/10.1038/nature03185.

[8] M.D. Swaine, T. Beer, Explosive seed dispersal in hura crepitans L. (Euphorbiaceae), New Phytol. 78 (1977) 695–708, http://dx.doi.org/10.1111/j.1469-8137.1977.tb02174.x.

[9] E. Katifori, S. Alben, E. Cerda, D.R. Nelson, J. Dumais, Foldable structures and the natural design of pollen grains, Proc. Natl. Acad. Sci. USA 107 (2010) 7635–7639, http://dx.doi.org/10.1073/pnas.0911223107.

[10] C. Dawson, J.F. Vincent, A.M. Rocca, How pine cones open, Nature 390 (1997) 668, http://dx.doi.org/10.1038/37745.

[11] R. Elbaum, L. Zaltzman, I. Burgert, P. Fratzl, The role of wheat awns in the seed dispersal unit, Science 316 (2007) 884–886, http://dx.doi.org/10.1126/science.1140097.

[12] S. Armon, E. Efrati, R. Kupferman, E. Sharon, Geometry and mechanics in the opening of chiral seed pods, Science 333 (2011) 1726–1730, http://dx.doi.org/10.1126/science.1203874.

[13] W. Jung, W. Kim, H.-Y. Kim, Self-burial mechanics of hygroscopically responsive awns, Integr. Comp. Biol. 54 (2014) 1034–1042, http://dx.doi.org/10.1093/icb/icu026.

[14] W. Jung, S.M. Choi, W. Kim, H.-Y. Kim, Reduction of granular drag inspired by self-burrowing rotary seeds, Phys. Fluids 29 (2017) 041702, http://dx.doi.org/10.1063/1.4979998.

[15] D. Evangelista, S. Hotton, J. Dumais, The mechanics of explosive dispersal and self-burial in the seeds of the filaree, Erodium cicutarium (Geraniaceae), J. Exp. Biol. 214 (2011) 521–529, http://dx.doi.org/10.1242/jeb.050567.

[16] C. Zhao, Q. Liu, L. Ren, Z. Song, J. Wang, A 3D micromechanical study of hygroscopic coiling deformation in Pelargonium seed: from material and mechanics perspective, J. Mater. Sci. 52 (2017) 415–430, http://dx.doi.org/10.1007/s10853-016-0341-6.

[17] R. Elbaum, Y. Abraham, Insights into the microstructures of hygroscopic movement in plant seed dispersal, Plant Sci. 223 (2014) 124–133, http://dx.doi.org/10.1016/j.plantsci.2014.03.014.

[18] Y. Abraham, R. Elbaum, Quantification of microfibril angle in secondary cell walls at sub-cellular resolution by means of polarized light microscopy, New Phytol. 197 (2013) 1012–1019, http://dx.doi.org/10.1111/nph.12070.

[19] H. Aharoni, Y. Abraham, R. Elbaum, E. Sharon, R. Kupferman, Emergence of spontaneous twist and curvature in non-euclidean rods: application to Erodium plant cells, Phys. Rev. Lett. 108 (2012) 238106, http://dx.doi.org/10.1103/PhysRevLett.108.238106.

[20] A. Rafsanjani, M. Stiefel, K. Jefimovs, R. Mokso, D. Derome, J. Carmeliet, Hygroscopic swelling and shrinkage of latewood cell wall micropillars reveal ultrastructural anisotropy, J. R. Soc. Interface 11 (2014) 20140126, http://dx.doi.org/10.1098/rsif.2014.0126.

[21] Y. Abraham, C. Tamburu, E. Klein, J.W. Dunlop, P. Fratzl, U. Raviv, R. Elbaum, Tilted cellulose arrangement as a novel mechanism for hygroscopic coiling in the stork's bill awn, J. R. Soc. Interface 9 (2012) 640–647, http://dx.doi.org/10.1098/rsif.2011.0395.

[22] I. Burgert, P. Fratzl, Actuation systems in plants as prototypes for bioinspired devices, Phil. Trans. R. Soc. A 367 (2009) 1541–1557, http://dx.doi.org/10.1098/rsta.2009.0003.

[23] R. Elbaum, S. Gorb, P. Fratzl, Structures in the cell wall that enable hygroscopic movement of wheat awns, J. Struct. Biol. 164 (2008) 101–107, http://dx.doi.org/10.1016/j.jsb.2008.06.008.

[24] Y. Abraham, R. Elbaum, Hygroscopic movements in Geraniaceae the structural variations that are responsible for coiling or bending, New Phytol. 199 (2013) 584–594, http://dx.doi.org/10.1111/nph.12254.

[25] R.M. Christensen, Mechanics of Composite Materials, Wiley, New York, 1979.

[26] J.N. Reddy, Theory and Analysis of Elastic Plates and Shells, Taylor & Francis, Philadelphia, 1999.

[27] L. Liu, S. Jiang, Y. Sun, S. Agarwal, Giving direction to motion and surface with ultra-fast speed using oriented hydrogel fibers, Adv. Funct. Mater. 26 (2016) 1021–1027, http://dx.doi.org/10.1002/adfm.201503612.

[28] D. Li, Y. Xia, Electrospinning of nanofibers: reinventing the wheel? Adv. Mater. 16 (2004) 1151–1170, http://dx.doi.org/10.1002/adma.200400719.

[29] B. Shin, J. Ha, M. Lee, K. Park, G.H. Park, T.H. Choi, K.-J. Cho, H.-Y. Kim, Hygrobot: a self-locomotive ratcheted actuator powered by environmental humidity, Sci. Robot. 3 (2018) eaar2629, http://dx.doi.org/10.1126/scirobotics.aar2629.

[30] J.R. Kalnin, E. Kotomin, Modified Maxwell–Garnett equation for the effective transport coefficients in inhomogeneous media, J. Phys. A 31 (1998) 7227–7234, http://dx.doi.org/10.1088/0305-4470/31/35/004.

Supplementary Material for "Hygroresponsive coiling of seed awns and soft actuators"

by Jonghyun Ha, Sung Mok Choi, Beomjune Shin, Minhee Lee, Wonjong Jung, and Ho-Young Kim

1. Mechanical description of composite plates

Matrices of the extensional stiffness $\boldsymbol{A}$, the coupling stiffness $\boldsymbol{B}$, and the bending stiffness $\boldsymbol{D}$ can be expressed as

$$\boldsymbol{A} = \sum_{k=1}^{n} \bar{\mathbf{D}}_k (z_{k+1} - z_k),$$

$$\boldsymbol{B} = \frac{1}{2}\sum_{k=1}^{n} \bar{\mathbf{D}}_k ({z_{k+1}}^2 - {z_k}^2),$$

$$\boldsymbol{D} = \frac{1}{3}\sum_{k=1}^{n} \bar{\mathbf{D}}_k ({z_{k+1}}^3 - {z_k}^3).$$

Here, the stiffness matrix $\bar{\mathbf{D}}$ is

$$\bar{\mathbf{D}} = \frac{E}{1-\nu^2}\begin{bmatrix} 1 & \nu & 0 \\ \nu & 1 & 0 \\ 0 & 0 & (1-\nu)/2 \end{bmatrix},$$

where the material is assumed to be isotropic with E and ν being respectively Young's modulus and Poisson's ratio. The awn model is composed of three layers, and thus $n = 4$ as shown in Fig. 2a. Our artificial actuator consists of two layers, one hygroscopically active and the other inactive as shown in Fig. 3c, and thus $n = 3$.

The hygroscopic expansion coefficient vector $\boldsymbol{\alpha}$ should be considered from the reference coordinates:

$$\boldsymbol{\alpha} = \mathbf{R}\mathbf{H}^{-1}\mathbf{R}^{-1}\begin{Bmatrix} \alpha_1 \\ \alpha_2 \\ 0 \end{Bmatrix},$$

where $\mathbf{H}$ and $\mathbf{R}$ are transformation matrix and Reuter's matrix, respectively:

$$\mathbf{H} = \begin{bmatrix} \cos\theta^2 & \sin^2\theta & 2\sin\theta\cos\theta \\ \sin^2\theta & \cos^2\theta & -2\sin\theta\cos\theta \\ -\sin\theta\cos\theta & \sin\theta\cos\theta & \cos^2\theta - \sin^2\theta \end{bmatrix},$$

$$\mathbf{R} = \begin{bmatrix} 1 & 0 & 0 \\ 0 & 1 & 0 \\ 0 & 0 & 2 \end{bmatrix}.$$

The expansion coefficients α_1 and α_2 correspond to the material coordinates 1 and 2, respectively. When we rotate the reference coordinates (x, y) by $\pi/2 - \theta$ to coincide with the material coordinates $(1, 2)$, $\boldsymbol{\alpha}$ of the reference coordinates can be calculated by the above equation.

2. Helical deformation due to hygroscopic responses

We write $\mathbf{N}$ and $\mathbf{M}$ (per unit width) induced by hygroscopic swelling as

$$\mathbf{N} = \int \boldsymbol{\sigma_h} \mathrm{d}z = \int \bar{\mathbf{D}} \boldsymbol{\alpha} \Delta\phi \mathrm{d}z,$$

$$\mathbf{M} = \int \boldsymbol{\sigma_h} z \mathrm{d}z = \int \bar{\mathbf{D}} \boldsymbol{\alpha} \Delta\phi z \mathrm{d}z,$$

where $\boldsymbol{\sigma_h}$ is the hygroscopic stress. Now the integrations of $\mathbf{N}$ and $\mathbf{M}$ are simplified to

$$\mathbf{N} = \sum_{k=1}^{n} \bar{\mathbf{D}}_k \boldsymbol{\alpha}_k \Delta\phi (z_{k+1} - z_k),$$

$$\mathbf{M} = \frac{1}{2} \sum_{k=1}^{n} \bar{\mathbf{D}}_k \boldsymbol{\alpha}_k \Delta\phi ({z_{k+1}}^2 - {z_k}^2),$$

which allow us to find forces and moments acting on the trilayer as a function of $\Delta\phi$ when the mechanical properties are given.

The strain and curvature vector are obtained based on $\mathbf{N}$ and $\mathbf{M}$ as

$$\begin{Bmatrix} \boldsymbol{\epsilon_0} \\ \boldsymbol{\kappa} \end{Bmatrix} = \begin{bmatrix} \boldsymbol{A} & \boldsymbol{B} \\ \boldsymbol{B} & \boldsymbol{D} \end{bmatrix}^{-1} \begin{Bmatrix} \mathbf{N} \\ \mathbf{M} \end{Bmatrix}.$$

Here, the inverse matrix is written as

$$\begin{bmatrix} \boldsymbol{A} & \boldsymbol{B} \\ \boldsymbol{B} & \boldsymbol{D} \end{bmatrix}^{-1} = \begin{bmatrix} {\boldsymbol{S}_\mathrm{D}}^{-1} & -{\boldsymbol{S}_\mathrm{A}}^{-1} \boldsymbol{B} \boldsymbol{D}^{-1} \\ -\boldsymbol{D}^{-1} \boldsymbol{B} {\boldsymbol{S}_\mathrm{D}}^{-1} & {\boldsymbol{S}_\mathrm{A}}^{-1} \end{bmatrix},$$

where $\boldsymbol{S}_\mathrm{D} = \boldsymbol{A}^{-1} - \boldsymbol{B}\boldsymbol{D}^{-1}\boldsymbol{B}$ and $\boldsymbol{S}_\mathrm{A} = \boldsymbol{D}^{-1} - \boldsymbol{B}\boldsymbol{A}^{-1}\boldsymbol{B}$. Thus, the curvature vector is given by

$$\boldsymbol{\kappa} = -\boldsymbol{D}^{-1} \boldsymbol{B} {\boldsymbol{S}_\mathrm{D}}^{-1} \mathbf{N} + {\boldsymbol{S}_\mathrm{A}}^{-1} \mathbf{M} = \begin{Bmatrix} \kappa_x \\ \kappa_y \\ \kappa_{xy} \end{Bmatrix}.$$

The curvature vector can transform to the matrix form:

$$\bar{\boldsymbol{b}}^{*} = \begin{bmatrix} \kappa_x & \kappa_{xy} \\ \kappa_{xy} & \kappa_y \end{bmatrix}.$$

We find the eigenvalues λ ($= \kappa_1,\ \kappa_2$) of the curvature tensor $\bar{\boldsymbol{b}}^{*}$ by using $|\bar{\boldsymbol{b}}^{*} - \lambda \boldsymbol{I}| = 0$. Then the reference curvature tensor $\bar{\boldsymbol{b}}$ is obtained as in Eq. (1). Based on κ_0, the helix configuration is reproduced via the reconstruction function [1]:

$$\Psi(u,\ v) = \frac{1}{\beta}\left[\kappa \cos\left(\beta u - \frac{\tau\beta}{\kappa} v\right),\ \kappa \sin\left(\beta u - \frac{\tau\beta}{\kappa} v\right),\ \tau\beta u + \kappa\beta v\right],$$

where $\kappa = \kappa_0 \cos^2\psi$, $\tau = \kappa_0 \cos\psi \sin\psi$, $\beta = \kappa^2 + \tau^2$, and u and v are the lengthwise and widthwise coordinates of the parametric curves.

3. Mechanical properties and dimensions of the seed awns and the actuators

Properties & dimensions	Seed awn	Actuator
Young's modulus, E_{a}	86 GPa	135 MPa
Shear modulus, G_{a}	66 GPa	108 MPa
Poisson's ratio, ν_{a}	0.3	0.25
Hygroscopic expansion coefficient, α_1	0.15 - 0.2	0.15
Hygroscopic expansion coefficient, α_2	0	0
Young's modulus, E_{i}	100 GPa	1 Gpa
Poisson's ratio, ν_{i}	0.04	0.34
Thickness, h_{a}	40 µm	40 µm
Thickness, h_{i}	30 µm	50 µm
Microfibril angle, θ	70 - 80°	-
Tilt angle, ψ	15 - 20°	various

Supplementary Table 1: Mechanical properties and dimensions of *Pelargonium appendiculatum* seed awns and the hygroscopic actuators. Subscripts a and i denote active and inactive layer, respectively. The numbers 1 and 2 are material coordinates. The elastic moduli of the awns are derived from literature values of basic botanical materials [2], and those of the actuators are measured by a testing device (Universal Testing Systems 3342, Instron). Hygroscopic expansion coefficients of the awns and actuators (PEO fibers), α, are measured in a thermo-hygrostat.

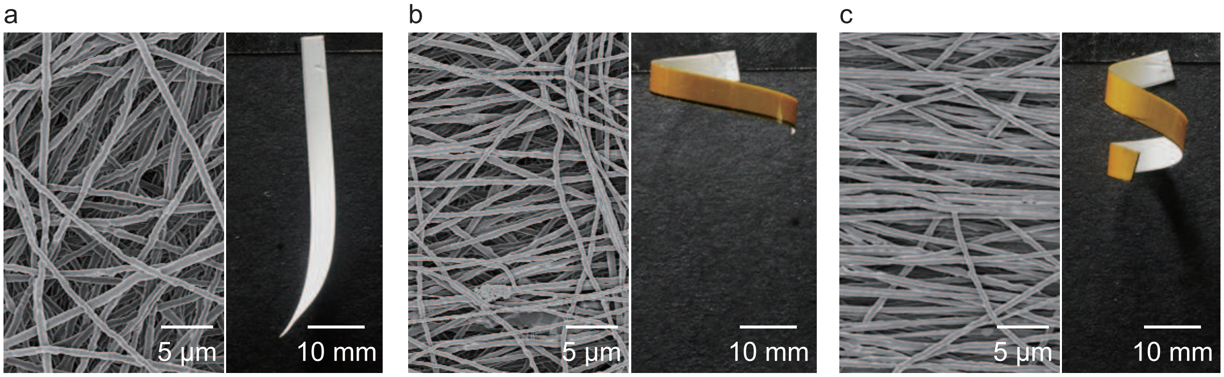

Supplementary Figure 1: Effects of rotational speed of collector on the microstructure of the active layer (left panel) and the helical shape of the bilayer (right panel) at RH=20%. The cutting angle $\psi = 20^\circ$ for all the bilayers. The rotational speed of collector is (a) 0, (b) 1000 rpm, and (c) 2000 rpm.

4. Effects of rotational speed of collector

In the electrospinning process to fabricate the active fibrous layer, we rotated the drum collector to directionally align the fibers. To investigate the effects of the rotational speed of collector on fiber alignment and the consequent actuation performance, we fabricated the active layer at the rotational speed of 0 and 1000 rpm. Then we compared their microstructure and helical shapes with those fabricated at 2000 rpm in Supplementary Fig. 1. At 2000 rpm, where the linear speeds of the collector surface and the jet coincide, the bilayer actuator coils to form a helix with the pitch and the radius agreeing with our theoretical model assuming one-directional elongation of the active layer. At 1000 rpm, which results in only partially aligned fibers, the bilayer strip cannot even make a full turn because the expansion of the active layer occurs in diverse directions thereby reducing effective bending moment. With a stationary collector resulting in a randomly deposited fibrous layer, the degree of actuation is very small, revealing the importance of aligning fibers in achieving effective bilayer actuators.

5. Effects of thickness on helical shape of artificial bilayers

In our analysis adopting the theory of thin laminated composite plates, the thickness of the active and the inactive layer affects the shape of the helix, i.e. pitch P and radius R. Supplementary Fig. 2 shows the computational results of P and R as a function of the thickness of each layer when the relative humidity RH=45%. We see that P and R decrease with the active layer thickness when h_a

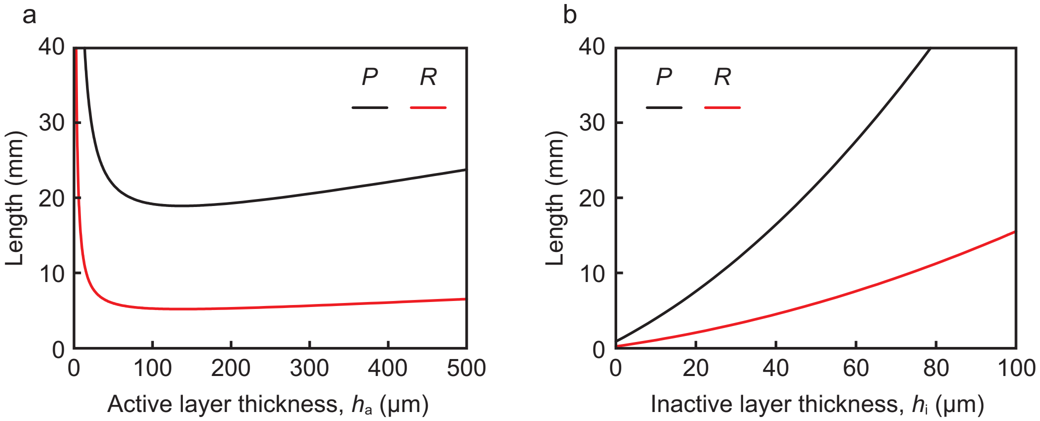

Supplementary Figure 2: Effects of thickness on the pitch P and the radius R of artificial bilayer actuators. (a) The computational results of R and P versus h_{a} when $h_{\mathrm{i}} = 50$ μm. (b) The computational results of R and P versus h_{i} when $h_{\mathrm{a}} = 40$ μm. In the computations, $\psi = 30°$, $E_{\mathrm{a}} = 135$ MPa, and $E_{\mathrm{i}} = 1$ GPa.

is small, but they gradually increase after reaching their minima. Although the initial increase of h_{a} increases the bending moment, resulting in the decrease P and R, further increase of h_{a} rather increases the bending stiffness more rapidly, thus leading to the gradual increase of P and R. The thickness of the inactive layer, h_{i}, is only associated with the stiffness, and thus its increase naturally leads to the monotonous increase of P and R.

6. Applications for self-burrowing actuators

Inspired by the self-burial behavior of the *Pelargonium* seeds using their awns, which is the original purpose of the seeds having the awns, here we demonstrate that our artificial actuator can dig in soil as the environmental humidity increases. Supplementary Fig. 3 shows the sequential images of the bilayer actuator digging in a pile of glass beads of 370 μm in average diameter. The actuator is anchored at one end above the pile and the other end penetrates into the substrate by uncurling with the increase of environmental humidity. Such screwing actuation of the helical actuators can be utilized in future applications of self-digging sensors, robots [3] and smart dusts [4].

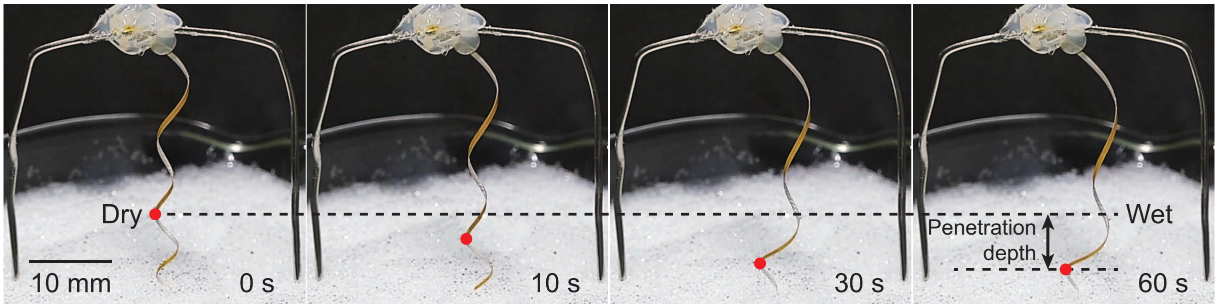

Supplementary Figure 3: A hygroscopic self-burrowing actuator activated by environmental humidity. The red point descends as the coiled bilayer actuator stretches out and penetrates the granular substrate with the increase of humidity.

References

[1] M. P. D. Carmo, Differential Geometry of Curves and Surfaces, Prentice-Hall, New Jersey, 1976.

[2] L. J. Gibson, The hierarchical structure and mechanics of plant materials, J. R. Soc. Interface 9 (2012) 2749-2766. https://doi.org/10.1098/rsif.2012.0341.

[3] A. A. Calderón, J. C. Ugalde, J. C. Zagal and N. O. Pérez-Arancibia, Design, fabrication and control of a multi-material-multi-actuator soft robot inspired by burrowing worms, In Proceedings of the 2016 IEEE International Conference on Robotics and Biomimetics (2016) 31–38. https://doi.org/10.1109/ROBIO.2016.7866293.

[4] B. Warneke, M. Last, B. Liebowitz and K. S. Pister, Smart dust: Communicating with a cubic-millimeter computer. Computer 34 (2001) 44-51. https://doi.org/10.1109/2.895117.